









Multiple magnetic orders in $\text{LaFeAs}_{1-x}\text{P}_x\text{O}$ uncover universality of iron-pnictide superconductors

Ryan Stadel ^{1,2,6}, Dmitry D. Khalyavin³, Pascal Manuel ³, Koji Yokoyama ³, Saul Lapidus⁴, Morten H. Christensen^{5,7}, Rafael M. Fernandes ⁵, Daniel Phelan¹, Duck Young Chung ¹, Raymond Osborn ¹, Stephan Rosenkranz ¹ & Omar Chmaissem ^{1,2}✉

The iron-pnictide superconductors have generated tremendous excitement as the competition between magnetism and superconductivity has allowed unique in-roads towards elucidating a microscopic theory of unconventional high-temperature superconductivity. In addition to the stripe spin density wave (C_{2M}^a) phase observed in the parent compounds of all iron-pnictide superconductors, two novel magnetic orders have recently been discovered in different parent structures: an out-of-plane collinear double- \mathbf{Q} (C_{4M}^c) structure in the hole-doped $(\text{Ca}, \text{Sr}, \text{Ba})_{1-x}(\text{Na})_x\text{Fe}_2\text{As}_2$ and $\text{Ba}_{1-x}\text{K}_x\text{Fe}_2\text{As}_2$ families, and a spin vortex crystal “hedgehog” (C_{4M}^{ab}) structure in the $\text{CaKFe}_4\text{As}_4$ family. Using neutron diffraction, we demonstrate that $\text{LaFeAs}_{1-x}\text{P}_x\text{O}$ contains all three magnetic orders within a single-phase diagram as a function of substitution, all of which compete strongly with superconductivity. Our experimental observations combined with theoretical modeling demonstrate how the reduction in electronic correlations by chemical substitution results in larger Fermi surfaces and the sequential stabilization of multiple magnetic anisotropies. Our work presents a unified narrative for the competing magnetic and superconducting phases observed in various iron-pnictide systems with different crystal structures and chemistry.

¹Materials Science Division, Argonne National Laboratory, Lemont, IL 60439, USA. ²Physics Department, Northern Illinois University, DeKalb, IL 60115, USA. ³ISIS Pulsed Neutron and Muon Source, Rutherford Appleton Laboratory, Chilton, Didcot OX11 0QX, UK. ⁴Advanced Photon Source, Argonne National Laboratory, Lemont, IL 60439, USA. ⁵School of Physics and Astronomy, University of Minnesota, Minneapolis, MN 55455, USA. ⁶Present address: Chemistry and Biochemistry, University of Maryland, College Park, MD 20742, USA. ⁷Present address: Center for Quantum Devices, Niels Bohr Institute, University of Copenhagen, 2100 Copenhagen, Denmark. ✉email: chmaissem@anl.gov

With the discovery of superconductivity (SC) in the iron-based compound $\text{LaFeAsO}_{1-x}\text{F}_x$ in 2008¹, a fascinating new class of materials joined the cuprates as a pristine frontier to further explore unconventional superconductivity and help elucidate the origin of high-temperature superconductors. This was the first family of iron-based superconductors, now referred to as 1111 compounds, but they were followed quickly by the discovery of SC in the related hole-doped $\text{Ba}_{1-x}\text{K}_x\text{Fe}_2\text{As}_2$ ² and electron-doped $\text{Ba}(\text{Fe}_{1-x}\text{Co}_x)_2\text{As}_2$ ^{3,4} (122 family). Both families exhibit in-plane, two-fold rotationally symmetric stripe antiferromagnetic order (C_{2M}^a) in their respective unsubstituted parent compounds⁵. Subsequently, superconductivity was discovered in the NaFeAs ⁶ (111) system, as well as the CaFe_4As_4 ($A = \text{K, Rb, Cs}$) and SrFe_4As_4 ($A = \text{Rb, Cs}$)⁷ (1144) compounds. These systems all either exhibit antiferromagnetic ordering in their parent compound or become magnetically ordered upon small doping concentrations with superconductivity arising at the phase boundaries as this magnetic order is suppressed by chemical substitution or pressure⁸. This proximity of SC to magnetic order, analogous to the cuprates and heavy fermions, suggests unconventional superconducting pairing which was indeed demonstrated theoretically^{9–12} and experimentally¹³. Extensive research further led to the discovery of additional exotic magnetic states such as the re-entrant tetragonal C_{4M}^c out-of-plane collinear double-Q magnetic phase universally observed in the hole-doped 122s^{14–18} and the in-plane non-collinear double-Q spin vortex crystal “hedgehog” (C_{4M}^{ab}) ordering identified in $\text{CaKFe}_4\text{As}_4$ ^{19,20} as well as suggested for $\text{Ba}_{1-x}\text{Na}_x\text{Fe}_2\text{As}_2$ ²¹. The magnetic phases are shown in Fig. 1b: the notation C_{2M}^a , C_{4M}^{ab} , and C_{4M}^c refers to the distinguishing attributes of rotational symmetry (with the subscript denoting whether the magnetic ordered state has two-fold or four-fold symmetry) and in- or out-of-plane spins (with the superscript denoting the magnetization direction). The possibility of the iron-pnictides realizing three distinct magnetic phases was proposed by Lorenzana et al.²², and their microscopic origin has been attributed to a range of effects, such as poorer nesting conditions^{23,24}, spin-orbit coupling^{25,26}, disorder²⁷, and quantum fluctuations²⁸. Whether these seemingly unrelated magnetic orders are idiosyncrasies of their respective systems or an indicator of underlying general behavior remains an open question necessitating the exploration of additional frameworks such as the under-investigated 1111 system.

The RFePnO family, where R is a rare earth and Pn is a pnictogen (typically arsenic or phosphorus), exhibits a rich phase diagram. Non-structural probes (e.g., NMR, resistivity, and magnetic susceptibility) have suggested the possible existence of unknown magnetic states in $\text{LaFeAs}_{1-x}\text{P}_x\text{O}$ ^{29–33}, but determination of magnetic order on the iron sublattice has only been performed in the parent LaFeAsO , where C_{2M}^a order was observed^{34–36}. The full $\text{LaFeAs}_{1-x}\text{P}_x\text{O}$ phase diagram is complex with multiple magnetic states and two disconnected superconducting domes forming a unique pattern over at least four distinct regions³⁷. Such separated islands of superconductivity have not been observed in any other pnictide series, thus making $\text{LaFeAs}_{1-x}\text{P}_x\text{O}$ a prime ground for in-depth exploration of these competing states.

At first glance, the unique superconducting features of the $\text{LaFeAs}_{1-x}\text{P}_x\text{O}$ system seem a significant departure from the related 122 and 1144 families. However, substitution of fluorine^{31,33,38} for oxygen was shown to completely suppress³⁰ all magnetic orders and to extend superconductivity over the entire phosphorus-substituted phase diagram. The merging of the two SC domes demonstrates that they are remnants of a single state that had been suppressed by competing magnetic orders. Partial depression of T_c was also seen in the hole-doped 122s in conjunction with the emergence of the C_{4M}^c phase³⁹. These

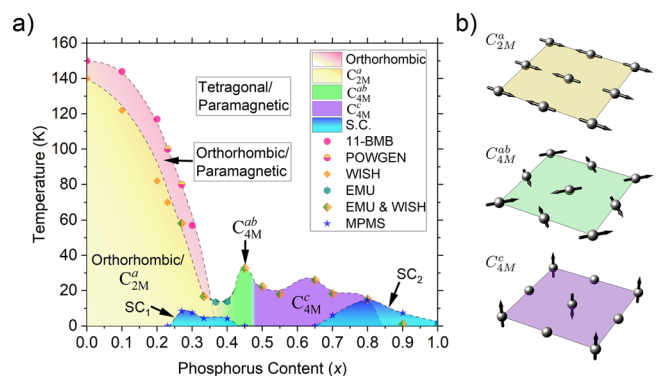


Fig. 1 Phase diagram with magnetic structures. **a** Here we present our structural and magnetic phase diagram. Neutron diffraction from WISH was used to identify the magnetic structures, while muon spin relaxation (μSR) at EMU was performed on the same samples to identify the transition temperatures, due to much faster counting time for μSR . As x increases, the system's magnetic order evolves from two-fold symmetric with moments along a , C_{2M}^a , to four-fold symmetric with moments along both a and b , C_{4M}^{ab} , to four-fold symmetric with moments out-of-plane along c , C_{4M}^c , for which the structure can be visualized in **b**. The single-Q structure with orthorhombic symmetry in C_{2M}^a becomes a double-Q structure in C_{4M}^{ab} as the nuclear structure adopts a tetragonal symmetry. The diagonal moments in the C_{4M}^{ab} order are a consequence of a superposition of two orthogonal “copies” of the C_{2M}^a that arise as the system becomes tetragonal so that the lattice parameters a and b become equivalent. Likewise, the C_{4M}^c is a result of two parallel “copies” of out-of-plane spin density waves that constructively and destructively interfere to produce the magnetic pattern seen, where half of the sites have a double moment, and the other half have none. Superconducting transition temperatures were determined by the global minimum in the 2nd derivative of magnetic susceptibility measurements performed on a Quantum Design MPMS.

observations hint at an underlying universal behavior common to the 1111 and 122 systems, but conclusive comparisons require solving the magnetic structures in the 1111s.

Here, we present a detailed investigation of structural and magnetic order in 1111 compounds utilizing synchrotron x-ray and neutron diffraction and muon spin relaxation (μSR). We find that unlike any other family of compounds, the $\text{LaFeAs}_{1-x}\text{P}_x\text{O}$ series exhibits direct paramagnetic-to-magnetic transitions to all three types of magnetic orders, orthorhombic single-Q C_{2M}^a , tetragonal in-plane double-Q C_{4M}^{ab} , (as observed in 1144s), and tetragonal out-of-plane double-Q C_{4M}^c (as observed in hole-doped 122s) within the same phase diagram, Fig. 1a. Supplementary Figure 1 displays high-resolution synchrotron x-ray data demonstrating the tetragonal character within experimental resolution of the double-Q magnetic phases ($x > 0.35$). A key difference to emphasize is that in 122s, the C_{4M}^c exists within the overlapping region between the C_{2M}^a and SC domes, whereas in $\text{LaFeAs}_{1-x}\text{P}_x\text{O}$ the tetragonal magnetic order is observed outside of the C_{2M}^a . Using a microscopic model in which the isovalent chemical substitution of phosphorus for arsenic is described by an increase in the size of the Fermi surface, see Christensen et al.²⁵, we reproduce the hierarchy of magnetic phases, with C_{2M}^a order being favored by small Fermi surfaces, while successively larger Fermi surfaces yield first a C_{4M}^{ab} phase followed by a C_{4M}^c phase. Here, spin-orbit coupling is a necessary ingredient to solve a degeneracy between the tetragonal magnetic phases, reproducing the observed consecutive reorientations of the magnetic moments.

Results and discussion

We have conducted a detailed survey of the phase diagram of $\text{LaFeAs}_{1-x}\text{P}_x\text{O}$ using high-resolution synchrotron x-ray powder

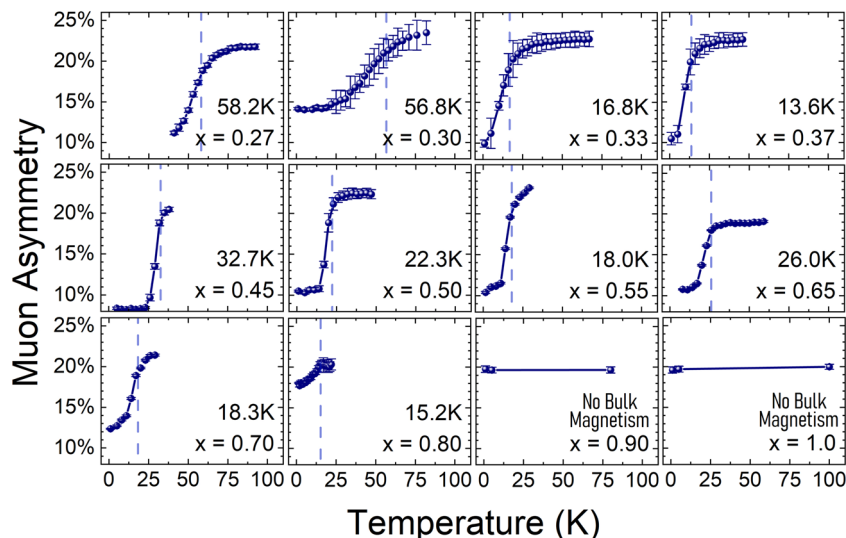


Fig. 2 Results of fits to muon spin relaxation (μ SR) data collected on EMU. Summation of refined asymmetry amplitude with each blue circle representing the value of the longitudinal relaxation, $G_z(t)$, modeled as a stretched exponential of the form $G_z(t) = A_0 + A_1 e^{-(\lambda t)^\beta}$ at $t = 0$ s for the given temperature. A_0 , A_1 , λ , and β are all constants to model the exponential decay of the detected asymmetry (the difference in positrons produced in muon decay between the front and back detectors) as a function of time, t . The vertical dashed line represents magnetic transition temperatures defined by the inflection point in the 2nd derivative of the magnetization curve. Constant asymmetry values above 20% are expected for non-magnetic samples. When asymmetry drops to ~8–12%, a sample is exhibiting bulk magnetism^{70,71}. The error bars are reported from the asymmetry amplitude fit performed using the Mantidplot software⁶⁷.

diffraction, neutron diffraction, and μ SR. Details of the synthesis and characterization of the polycrystalline samples are presented in the methods section.

We observe a continuous sequence of the three distinct magnetic phases shown in Fig. 1b, which previously have not been observed to occur in a single-phase diagram as a function of substitution in any other pnictide system. The evolution of the magnetic order with increasing phosphorus substitution begins as orthorhombic single-Q C_{2M}^a order, followed by two back-to-back tetragonal double-Q magnetic phases: the in-plane C_{4M}^{ab} “hedgehog” phase existing over a narrow range around $x = 0.45$, and the out-of-plane C_{4M}^c order covering a wide range of phosphorus content from $0.5 \leq x \leq 0.8$. Interestingly, the C_{4M}^{ab} phase seems to play the role of an intermediate phase while switching from the in-plane C_{2M}^a to the out-of-plane C_{4M}^c magnetic states.

Experimental data and analysis. Our magnetic susceptibility measurements show superconducting transitions in agreement with the literature^{30,40}. Prior to this work, ^{31}P -NMR (phosphorus nuclear magnetic resonance) studies^{29,30,32} had reported the Néel temperatures (T_N) for the C_{2M}^a phase for $x \leq 0.2$ and provided evidence for unknown magnetic order in the substitution range of $0.4 \leq x \leq 0.7$. Our μ SR measurements show evidence of bulk magnetism for every sample with $x \leq 0.8$, Fig. 2. Neutron diffraction was used to determine the structural details of the magnetic orders over the entire phase diagram. Supplementary Figure 2 displays refinements of the magnetic structure using various models for three representative samples ($x = 0.23$, 0.45 and 0.8). Agreement between measured magnetic transition temperatures from neutron diffraction and μ SR results was confirmed by performing temperature dependent scans for several of the same samples across both instruments. While our muon spin rotation experiment was crucial in determining the bulk magnetic properties of our samples, an in-depth analysis of the data from which the muon stopping sites could be identified requires short time scales that are inaccessible at the EMU beamline. We hope that this work motivates

future muon spin rotation and Mössbauer spectroscopy experiments to determine the bimodal local field distribution for the tetragonal magnetic phases.

A linear fit of the c-axis parameter refined using neutron and x-ray diffraction data is in agreement with Vegard’s law⁴¹, thereby confirming the successful systematic substitution of phosphorus for arsenic throughout our solid solution series, Fig. 3a. The unsubstituted parent end-members (LaFeAsO and LaFePO) display structural properties and lattice parameters in agreement with those reported in references⁴² and⁴³. Both x-ray and neutron diffraction confirmed the tetragonal to orthorhombic structural transition, up to $x = 0.35$, occurring at a slightly higher temperature than the C_{2M}^a magnetic transition, in agreement with previous studies on the 1111 systems^{42–49}. Figure 3a illustrates the continuous suppression with increasing x of the orthorhombic distortion at $T = 10$ K. The system is fully tetragonal for $x \gtrsim 0.35$.

Identification of the C_{2M}^a , C_{4M}^{ab} and C_{4M}^c magnetic orders is easily and unambiguously made by carefully examining the relative intensities and location in reciprocal space of their diffracted magnetic peaks. Very different diffraction angles and relative intensities are expected for the diverse magnetic states. As shown in Fig. 4, for example, the two most intense magnetic peaks for the C_{2M}^a phase are observed around 4.05 and 5.4 Å while those of the C_{4M}^{ab} phase are at 3.43 and 4.73 Å. Those of the C_{4M}^c are at 4.71 and 5.63 Å. Confirmation of the magnetic structures is further revealed from detailed Rietveld refinements using the appropriate models (please also see the Supplementary Figure 2). Examples of neutron diffraction data from each of the three magnetic states are presented in Fig. 4. Data from above (red lines) and below (blue lines) T_N are plotted together with their difference (purple lines). The magnetic and structural refinements were performed on the full low-temperature diffraction pattern while magnetic refinements were performed concurrently on the difference pattern. The tested magnetic models indexed the correct peaks and, upon refinement, match intensities and peak profiles appropriately with no extra

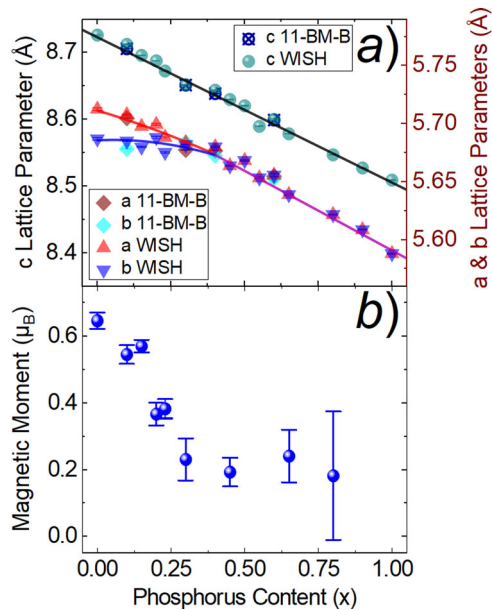


Fig. 3 Refined structural parameters and magnetic moments. **a** Each symbol represents the refined lattice parameter results as defined in the legend for $\text{LaFeAs}_{1-x}\text{P}_x\text{O}$ at $T = 10$ K. End points are in close agreement with lattice parameters reported in⁴² and⁴³. Solid lines are fits of the lattice parameters as follows: black line is a linear fit of the c-axis demonstrating adherence to Vegard's Law and a successful continuous substitution of phosphorus for arsenic. Red, blue, and purple lines serve as guides to the eye. **b** Magnetic moment refined from neutron diffraction as a function of substitution across the phase diagram. The refined error bars on the sample at $x = 0.8$ are large due to the small magnetic phase fraction in this particular sample. Note that a finite moment persists even when the lattice parameters a and b are equal, signaling the onset of four-fold rotationally symmetric magnetic order. Error bars are smaller than the symbol size for the lattice parameters. For the magnetic moments, error bars are those calculated by the Rietveld refinement programs.

intensities. The difference plot allows for an easier qualitative visual analysis of the very small magnetic peaks. The refined magnetic moments from neutron diffraction are shown in Fig. 3b. Phase fractions were identified from the nuclear refinement, and the magnetic phase fraction was matched to the main nuclear phase. The refined magnetic moment for $x = 0$ begins at $\sim 0.6 \mu_B$ in the C_{2M}^a regime, similar to that observed in the 122s, drops continuously to $\sim 0.2 \mu_B$ and remains roughly constant for compositions with $x \geq 0.3$. The refined magnetic moments were congruent with the observed magnetic Bragg reflection intensities, with Bragg peak magnitudes approximately scaling with the square of the moment, further indicating the positive identification of the magnetic phases.

Theoretical model. To understand the evolution of magnetism in this series, we note that all magnetic states observed here can be described in terms of two order parameters \mathbf{M}_1 and \mathbf{M}_2 that are related to the local magnetization $\mathbf{m}(\mathbf{R})$ according to:

$$\mathbf{m}(\mathbf{R}) = \mathbf{M}_1 \cos(\mathbf{Q}_1 \cdot \mathbf{R}) + \mathbf{M}_2 \cos(\mathbf{Q}_2 \cdot \mathbf{R}) \quad (1)$$

Here, $\mathbf{Q}_1 = (\pi, 0)$ and $\mathbf{Q}_2 = (0, \pi)$ are the antiferromagnetic wave-vectors in the 1Fe/unit cell. The nature of the magnetic instability is determined by the coefficients of the Landau free-

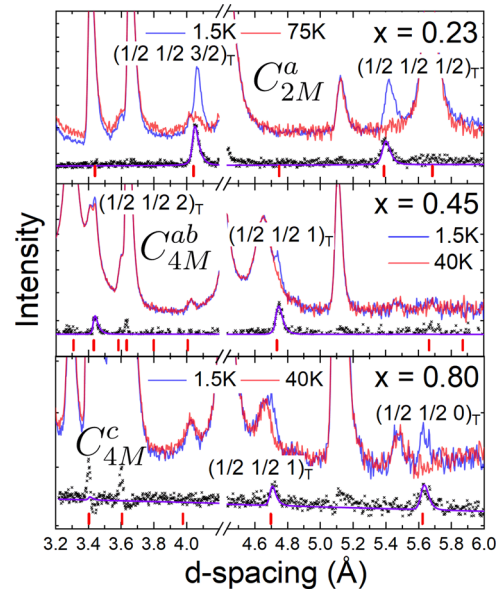


Fig. 4 Example neutron diffraction data showing magnetic Bragg reflections. Difference plots (black crosses) between neutron diffraction performed at temperatures above (red line) and below (blue line) magnetic transitions with magnetic Rietveld refinement plotted over difference (purple line). The two most intense magnetic peaks for each sample are labeled using the tetragonal unit cell notation. Representative examples of data for the three magnetic phases were selected. The peak at 5.7 \AA in the $x = 0.23$ sample is from an impurity, $\text{La}(\text{OH})_3$. The peaks at ~ 3.4 , and 4.6 \AA in the $x = 0.45$ and $x = 0.80$ samples are from LaOH . The lanthanum hydroxides are estimated from refinements at $\sim 1\%$ by weight. Red tick marks are symmetry-allowed magnetic Bragg reflections.

energy expansion $F(\mathbf{M}) = F^{(2)} + F^{(4)}$:

$$F^{(2)} = a(M_1^2 + M_2^2) + \alpha_1(M_{1,x}^2 + M_{2,y}^2) + \alpha_2(M_{2,x}^2 + M_{1,y}^2) + \alpha_3(M_{1,z}^2 + M_{2,z}^2) \quad (2)$$

$$F^{(4)} = \frac{u}{2}(M_1^2 + M_2^2)^2 - \frac{g}{2}(M_1^2 - M_2^2)^2 + 2w(\mathbf{M}_1 \cdot \mathbf{M}_2)^2 \quad (3)$$

The quadratic part of the expansion, $F^{(2)}$, in Eq. (2) has two parts: a spin-isotropic term, whose coefficient a determines the magnetic transition temperature, and a spin-anisotropic part, whose coefficients α_i select the direction of the magnetization. The quartic coefficients, Eq. (3), determine which magnetic order is favored^{22,50,51}. In particular, the C_{2M}^a phase, which corresponds to only one of the order parameters being non-zero, is favored by $g > 0$. On the other hand, $g < 0$ and $w > 0$ favor the C_{4M}^{ab} phase, corresponding to $|\mathbf{M}_1| = |\mathbf{M}_2|$ and $\mathbf{M}_1 \perp \mathbf{M}_2$, where $g < 0$ and $w < 0$ favor the C_{4M}^c phase, parametrized by $|\mathbf{M}_1| = |\mathbf{M}_2|$ and $\mathbf{M}_1 \parallel \mathbf{M}_2$.

Using a microscopic $k \cdot p$ model, a semi-empirical perturbation method for approximating the band-structure first derived by Cvetkovic et al.⁵², the coefficients of the Landau free energy were derived by Christensen et al.²⁵, providing a direct link between changes in microscopic parameters to changes in the magnetic ground state. Because in this approximation $w = 0$, the type of tetragonal magnetic phase selected for $g < 0$ is determined by the direction of the magnetization, which in turn is determined by the smallest α_i coefficient. For in-plane moments, which is the case when α_1 or α_2 is the smallest spin-anisotropic coefficient, the C_{4M}^{ab} phase is favored, while for out-of-plane moments, which is the

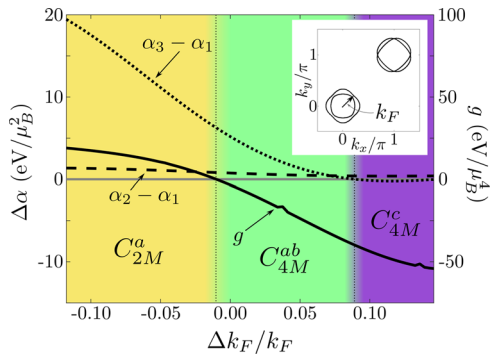


Fig. 5 Theoretical phase diagram. Evolution of Landau parameters α_i and g (constants from the quadratic and quartic parts of the Landau free energy expansion) as a function of change in Fermi momentum, $\Delta k_F/k_F$. This models the evolution of the leading magnetic instability with P substitution on the As site, with larger P concentrations corresponding to a larger Fermi surface. The left vertical axis represents the relative difference in these values for the constants, $\Delta\alpha$, and the right axis represents values for g . The transitions between different instabilities correspond to when g drops below zero and when $\alpha_3 - \alpha_1$ becomes smaller than $\alpha_2 - \alpha_1$. Inset is a snapshot of the Fermi surface in the 2Fe/unit cell.

case when α_3 is the smallest coefficient, the C_{4M}^c phase is the ground state.

To make contact with our experimental results, we need to model the impact of the isovalent chemical substitution on the band structure. To this end, we note that Dynamical Mean-Field Theory (DMFT) and Density Functional Theory (DFT) calculations indicate that LaFeAsO is more strongly correlated than LaFePO^{53,54}. One known effect of the correlations is to shrink the size of the Fermi pockets. This seems to be the case, for instance, in the related isovalently-substituted compounds Ba(Fe_{1-x}Ru_x)₂As₂ and Fe(Se_{1-x}S_x)^{55,56}. Thus, to proceed, we assume that the effect of phosphorus substitution is to increase the size of both electron and hole Fermi surfaces in our model (while keeping the total electronic occupation constant) and compute the Landau coefficients as a function of the change in the Fermi momentum $\frac{\Delta k_F}{k_F}$. While other effects may also contribute to the elucidation of our experimental data, we are confident that our simplified model provides useful insight to understand them. This is the main goal of the comparison between the theoretical and experimental results, and not to rule out other possible scenarios. Full details of our theoretical model are presented in the Supplementary Note 1 and Supplementary Figure 3.

Our results for g and α_i are shown in Fig. 5, using the general expressions derived by Christensen et al.²⁵ For relatively small Fermi surfaces, corresponding to the small x region of the phase diagram in our experiment, the magnetic ground state is the C_{2M}^a . As the Fermi surface area increases, corresponding to increasing phosphorus in our experiment, g becomes negative and the C_{4M}^{ab} phase is preferred, since α_1 is the smallest coefficient. Upon further increasing k_F , α_3 becomes the smallest coefficient, and the C_{4M}^c phase becomes the leading magnetic instability. We verified that this evolution of the coefficients is generic for a wide range of temperatures.

The stabilization of the C_{4M}^{ab} and C_{4M}^c phases splits the single superconducting dome, as seen by the recovery of a single SC dome with fluorine doping³⁰, into two disconnected domes. However, the highest temperature for any type of electronic order remains very stable across the phase diagram. Although the C_{4M}^c is a key feature occurring in a narrow region within the C_{2M}^a dome in the hole-doped 122s, it was not observed outside this dome as is the case in LaFeAs_{1-x}P_xO. The existence of a narrow C_{4M}^{ab} range, sandwiched between the much wider C_{2M}^a and C_{4M}^c

domes, implies a strong competition between the three states and superconductivity. The C_{4M}^{ab} phase has been observed in the 1144 system, which is an example of an A-site-ordered doubling along the c -axis of the 122 structure;⁵⁷ this establishes the host 122/1144 structure is capable of providing access to the C_{4M}^{ab} or the C_{4M}^c phase with such tuning. Our results uncover a previously hidden universality in magnetic ordering in close proximity to superconductivity. While it has been well-established that magnetism and superconductivity are intimately associated in the iron-pnictides, we demonstrate here that the C_{4M}^{ab} and C_{4M}^c are similarly related to SC. This universality is supported by a recent μ SR study in which Sheveleva et al.²¹ suggested the existence of the C_{4M}^{ab} phase in Ba_{1-x}Na_xFe₂As₂.

As to what is responsible for the progression of the diverse magnetic states, we note that the isovalent substitution of phosphorus is expected to modify the Fermi surface area^{55,56,58}. The theoretical model attributes the evolution of the magnetic ground states to the changes in the size of the Fermi surface which, in turn, is assumed to be driven by a suppression of correlations upon increasing the P content. Besides changes in the electronic structure, the emergence of disordered scattering centers caused by variations in ionic radius of the substituents also play a role. The disappearing and reappearing character of the superconducting domes suggests a tuning parameter that, rather than increasing monotonically, first increases and then decreases with x across the phase diagram; disorder could adopt this pattern as substitution across the phase diagram mirrors the ratio of whichever is dominant between arsenic and phosphorus around the $x = 0.5$ concentration.

Charge doping by fluorine or oxygen vacancies in this system has been shown to quickly suppress C_{2M}^a with a net positive effect on superconducting T_c ^{31,59,60}. Disorder (via isovalent chemical substitution), however, has a dual destructive effect on both T_c and T_N but suppresses C_{2M}^a at a faster rate than SC. This is because magnetism is suppressed^{61,62} by both inter and intraband scattering while only interband scattering is pair-breaking for the unconventional s^\pm superconducting state^{9,63–65}. Our results for LaFeAs_{1-x}P_xO are in agreement with this trend, since the ground state for $x = 0$ is C_{2M}^a . Introducing disorder by increasing x gradually suppresses the C_{2M}^a phase, allowing a relatively narrow SC dome to emerge between $x = 0.25$ and $x = 0.45$. At this crossroads, we observe a suppression of both T_N and T_c . We note similar suppression of T_N at the intersection between the C_{4M}^{ab} and C_{4M}^c at $x \approx 0.5$ and between the C_{4M}^c and SC at $0.7 < x < 0.8$. There is a clear symmetry in the phase diagram with the maximum T_c of both superconducting domes ($x \approx 0.27$ and $x \approx 0.8$) being approximately midway between the minimally disordered end members and the maximum disorder at $x = 0.5$. The C_{4M}^c and the C_{4M}^{ab} phases appear to be more resilient to disorder than the C_{2M}^a , in agreement with theoretical predictions²⁷.

The lack of long-range magnetic order in fully-substituted LaFePO ($x = 1$) explains the relatively robust superconducting dome on this side of the phase diagram when compared to the As side. The last feature left to account for is the relative suppression of T_c for phosphorus content above $x = 0.8$. A reduction in T_c is in line with LaFePO being a better metal with weaker electronic correlations than LaFeAsO⁶⁶. However, in a system with such fierce phase competition driving a complex phase diagram, other factors may be influencing the superconducting behavior.

Conclusions

We have presented the results of neutron, x-ray, and μ SR on a systematically substituted series of LaFeAs_{1-x}P_xO polycrystalline samples along with the most complete phase diagram to date, accounting for the evolution of the magnetic structures and their

relative placement with respect to superconductivity in this system. Our results highlight the simultaneous delicate balance and fierce competition between magnetism and superconductivity in a system in which all magnetic states known to the iron-pnictide family exist in the same compositional phase diagram. Our observation of C_{2M}^a , C_{4M}^{ab} , and C_{4M}^c in the 1111 and previously reported in the 122 and 1144 compounds uncovers a long-sought underlying generality of magnetic ordering in the iron-pnictides and the role it plays in relation to superconductivity. With a better understanding of the nature of the ground states and a theoretical model to explain their evolution, we have developed a framework through which to view a unified understanding of the interplay between superconductivity and magnetism in systems with different crystal structures and distinct types of chemical substitution.

Methods

Synthesis. Due to the toxic and carcinogenic properties of arsenic together with the air sensitivity of precursors, all synthesis was conducted inside an Ar-atmosphere glovebox with <5 ppm O₂ and <0.1 ppm H₂O. Initial synthesis of the powder samples was attempted following the procedures outlined by Lai et al.³⁰. However, due to its limitations in only being able to substitute up to $x = 0.66$, we developed a comprehensive recipe capable of producing high quality samples covering the full LaFeAs_{1-x}P_xO phase diagram as demonstrated by neutron and synchrotron diffraction.

Powder samples were prepared using LaAs, La₂O₃, LaP, Fe, Fe₂O₃, FeAs, Fe₂As, FeP, and Fe₂P precursors. Immediately prior to use, La₂O₃ was dried by heating overnight to 900 °C and placed inside an Ar-atmosphere glovebox after cooling to ~400 °C. Synthesis was carried out by thoroughly grinding precursors to a fine and well-mixed powder that was loaded into alumina crucibles. The alumina crucibles were flame sealed under vacuum inside quartz tubes. The samples were annealed at 1100 °C for up to 40 h. After each annealing cycle, the samples were checked for homogeneity by laboratory XRD until complete. Initial processes required up to four annealing cycles to achieve target purity, but the final procedure using Fe, Fe₂O₃, FeAs and FeP achieved homogeneity after only two cycles.

Experimental details. Quality of the samples was monitored after each synthesis step via laboratory x-ray diffraction on a PANalytical XRD. Magnetic and superconducting properties were measured in 10 Oe magnetic fields using a Quantum Design Magnetic Properties Measurement System (MPMS).

High resolution x-ray diffraction was performed for samples with $x = 0$ to $x = 0.6$ on beamline 11-BM-B at the Advanced Photon Source at Argonne National Laboratory. High resolution neutron diffraction was performed for samples ranging from $x = 0.23$ to $x = 1$ on POWGEN at the Spallation Neutron Source at Oak Ridge National Laboratory. High flux neutron diffraction was carried out for samples with $x = 0$ to $x = 0.8$ on WISH at ISIS at Rutherford Appleton Laboratory. μ SR was performed for samples of $x = 0.23$ to $x = 1$ on EMU at ISIS at RAL. The asymmetry from our measured temperature-dependent muon decay curves was quantified using Mantidplot⁶⁷ by a combined fit of a flat background and stretched exponential function with the form $G_z(t) = A_0 + A_1 e^{(-\lambda t)^\beta}$. This asymmetry was plotted as a function of temperature and the magnetic transition temperature T_N was extracted from second derivatives. Rietveld refinements were performed using the GSAS EXPGUI software suite⁶⁸ and GSAS-II⁶⁹.

Data availability

Neutron diffraction and muon resonance data used in this study are available from the corresponding author (OC) upon request.

Received: 22 October 2021; Accepted: 10 May 2022;

Published online: 14 June 2022

References

- Kamihara, Y., Watanabe, T., Hirano, M. & Hosono, H. Iron-based layered superconductor La[O_{1-x}F_x]FeAs ($x=0.05-0.12$) with $T_c=26$ K. *J. Am. Chem. Soc.* **130**, 3296 (2008).
- Rotter, M., Tegel, M. & Johrendt, D. Superconductivity at 38 K in the Iron Arsenide (Ba_{1-x}K_x)Fe₂As₂. *Phys. Rev. Lett.* **101**, 107006 (2008).
- Leithe-Jasper, A., Schnelle, W., Geibel, C. & Rosner, H. Superconducting state in SrFe_{2-x}Co_xAs₂ by internal doping of the iron arsenide layers. *Phys. Rev. Lett.* **101**, 207004 (2008).
- Sefat, A. S. et al. Superconductivity at 22 K in Co-doped BaFe₂As₂ Crystals. *Phys. Rev. Lett.* **101**, 117004 (2008).
- Rotter, M. et al. Spin-density-wave anomaly at 140 K in the ternary iron arsenide BaFe₂As₂. *Phys. Rev. B-Condens. Matter Mater. Phys.* **78**, 020503(R) (2008).
- Parker, D. R. et al. Structure, Antiferromagnetism and superconductivity of the layered iron arsenide NaFeAs. *Chem. Commun.* 2189–2191 (2009).
- Iyo, A. et al. New-structure-type Fe-based superconductors: CaFe₄As₄ (A=K, Rb, Cs) and SrFe₄As₄ (A=Rb, Cs). *J. Am. Chem. Soc.* **138**, 3410 (2016).
- Chen, X., Dai, P., Feng, D., Xiang, T. & Zhang, F. C. Iron-based high transition temperature superconductors. *Natl. Sci. Rev.* **1**, 371 (2014).
- Fernandes, R. M. et al. Unconventional pairing in the iron arsenide superconductors. *Phys. Rev. B-Condens. Matter Mater. Phys.* **81**, 140501 (2010).
- Mazin, I. I., Singh, D. J., Johannes, M. D. & Du, M. H. Unconventional superconductivity with a sign reversal in the order parameter of LaFeAsO_{1-x}F_x. *Phys. Rev. Lett.* **101**, 057003 (2008).
- Kuroki, K. et al. Unconventional pairing originating from the disconnected fermi surfaces of superconducting LaFeAsO_{1-x}F_x. *Phys. Rev. Lett.* **101**, 087004 (2008).
- Chubukov, A. V., Efremov, D. V. & Eremin, I. Magnetism, superconductivity, and pairing symmetry in iron-based superconductors. *Phys. Rev. B-Condens. Matter Mater. Phys.* **78**, 134512 (2008).
- Christianson, A. D. et al. Unconventional superconductivity in Ba_{0.6}K_{0.4}Fe₂As₂ from inelastic neutron scattering. *Nature* **456**, 930 (2008).
- Taddei, K. M. et al. Observation of the magnetic C₄ Phase in Ca_{1-x}Na_xFe₂As₂ and its universality in the hole-doped 122 superconductors. *Phys. Rev. B* **95**, 064508 (2017).
- Taddei, K. M. et al. Detailed magnetic and structural analysis mapping a robust magnetic C₄ Dome in Sr_{1-x}Na_xFe₂As₂. *Phys. Rev. B* **93**, 134510 (2016).
- Allred, J. M. et al. Tetragonal magnetic phase in Ba_{1-x}K_xFe₂As₂ from x-ray and neutron diffraction. *Phys. Rev. B-Condens. Matter Mater. Phys.* **92**, 094515 (2015).
- Avci, S. et al. Magnetically driven suppression of nematic order in an iron-based superconductor. *Nat. Commun.* **5**, 3845 (2014).
- Allred, J. M. et al. Double-Q spin-density wave in iron arsenide superconductors. *Nat. Phys.* **12**, 493 (2016).
- Meier, W. R. et al. Hedgehog spin-vortex crystal stabilized in a hole-doped iron-based superconductor. *Npj Quantum Mater.* **3**, 5 (2018).
- Ding, Q. P. et al. Hedgehog spin-vortex crystal antiferromagnetic quantum criticality in CaK(Fe_{1-x}Ni_x)₄As₄ revealed by NMR. *Phys. Rev. Lett.* **121**, 137204 (2018).
- Sheveleva, E. et al. Muon spin rotation and infrared spectroscopy study of Ba_{1-x}Na_xFe₂As₂. *Phys. Rev. B* **101**, 224515 (2020).
- Lorenzana, J., Seibold, G., Ortix, C. & Grilli, M. Competing orders in FeAs layers. *Phys. Rev. Lett.* **101**, 186402 (2008).
- Eremin, I. & Chubukov, A. V. Magnetic degeneracy and hidden metallicity of the spin-density-wave state in ferropnictides. *Phys. Rev. B-Condens. Matter Mater. Phys.* **81**, 024511 (2010).
- Gastiasoro, M. N. & Andersen, B. M. Competing magnetic Double- Q phases and superconductivity-induced reentrance of C₂ magnetic stripe order in iron pnictides. *Phys. Rev. B-Condens. Matter Mater. Phys.* **92**, 140506 (2015).
- Christensen, M. H., Kang, J., Andersen, B. M., Eremin, I. & Fernandes, R. M. Spin reorientation driven by the interplay between spin-orbit coupling and Hund's rule coupling in iron pnictides. *Phys. Rev. B-Condens. Matter Mater. Phys.* **92**, 214509 (2015).
- Christensen, M. H., Orth, P. P., Andersen, B. M. & Fernandes, R. M. Magnetic phase diagram of the iron pnictides in the presence of spin-orbit coupling: frustration between C₂ and C₄ magnetic phases. *Phys. Rev. B* **98**, 014523 (2018).
- Hoyer, M., Fernandes, R. M., Levchenko, A. & Schmalian, J. Disorder-promoted C₄ -symmetric magnetic order in iron-based superconductors. *Phys. Rev. B* **93**, 144414 (2016).
- Christensen, M. H., Orth, P. P., Andersen, B. M. & Fernandes, R. M. Emergent magnetic degeneracy in iron pnictides due to the interplay between spin-orbit coupling and quantum fluctuations. *Phys. Rev. Lett.* **121**, 057001 (2018).
- Kitagawa, S. et al. Relationship between superconductivity and antiferromagnetism in LaFe(As_{1-x}P_x)O revealed by ³¹P-NMR. *J. Phys. Soc. Jpn.* **83**, 23707 (2014).
- Lai, K. T. et al. Evolution of the phase diagram of LaFeP_{1-x}As_xO_{1-y}F_y ($y=0-0.1$). *Phys. Rev. B-Condens. Matter Mater. Phys.* **90**, 64504 (2014).
- Lu, W. et al. Superconductivity at 41.0 K in the F-doped LaFeAsO_{1-x}F_x. *Solid State Commun.* **148**, 168 (2008).
- Mukuda, H. et al. Emergence of novel antiferromagnetic order intervening between two superconducting phases in LaFe(As_{1-x}P_x)O: ³¹P-NMR studies. *J. Phys. Soc. Jpn.* **83**, 83702 (2014).
- Iimura, S. et al. Two-dome structure in electron-doped iron arsenide superconductors. *Nat. Commun.* **3**, 1 (2012).
- De La Cruz, C. et al. Magnetic order close to superconductivity in the iron-based layered LaO_{1-x}F_xFeAs systems. *Nature* **453**, 899 (2008).

35. Ishikado, M. et al. Evidence of Spin density wave in LaFeAsO, the parent material of the new Fe-Based oxypnictide superconductors, Eprint ArXiv:0809.5128v2 (2008). <https://doi.org/10.48550/arXiv.0809.5128>
36. Dong, J. et al. Competing orders and spin-density-wave instability in La(O_{1-x}F_x)FeAs. *EPL* **83**, 27006 (2008).
37. Engetsu, F. et al Reemergent phase of antiferromagnetic order in iron-based superconductor LaFe(As_{1-x}P_x)O probed by ³¹P-NMR. *J. Phys.: Conf. Ser.* **592**, 012072 (2014).
38. Ma, F. & Lu, Z. Y. Iron-based layered compound LaFeAsO is an antiferromagnetic semimetal. *Phys. Rev. B - Condens. Matter Mater. Phys.* **78**, 033111 (2008).
39. Wang, L. et al. Complex phase diagram of Ba_{1-x}Na_xFe₂As₂: a multitude of phases striving for the electronic entropy. *Phys. Rev. B* **93**, 14514 (2016).
40. Wang, C. et al. Superconductivity in LaFeAs_{1-x}P_xO: Effect of chemical pressures and bond covalency. *EPL* **86**, 47002 (2009).
41. Denton, A. R. & Ashcroft, N. W. Vegard's Law. *Phys. Rev. A* **43**, 3161 (1991).
42. Qureshi, N. et al. Crystal and magnetic structure of the oxypnictide superconductor LaFeAsO_{1-x}F_x: A neutron-diffraction study. *Phys. Rev. B-Condens. Matter Mater. Phys.* **82**, 184521 (2010).
43. McQueen, T. M. et al. Intrinsic properties of stoichiometric LaFePO. *Phys. Rev. B-Condens. Matter Mater. Phys.* **78**, 24521 (2008).
44. Zhao, J. et al. Structural and magnetic phase diagram of CeFeAsO_(1-x)F_(x) and its relation to high-temperature superconductivity. *Nat. Mater.* **7**, 953 (2008).
45. Zhao, J. et al. Lattice and magnetic structures of PrFeAsO, PrFeAsO_{0.85}F_{0.15}, and PrFeAsO_{0.85}. *Phys. Rev. B-Condens. Matter Mater. Phys.* **78**, 132504 (2008).
46. Qiu, Y. et al. Crystal structure and antiferromagnetic order in NdFeAsO_{1-x}F_x (x=0.0 and 0.2) superconducting compounds from neutron diffraction measurements. *Phys. Rev. Lett.* **101**, 1 (2008).
47. Drew, A. J. et al. Coexistence of static magnetism and superconductivity in SmFeAsO_{1-x}F_x as revealed by muon spin rotation. *Nat. Mater.* **8**, 310 (2009).
48. Luo, Y. et al. Thorium-doping induced high-T_c superconductivity in Dy_{1-x}Th_xFeAsO. *Int. J. Mod. Phys. B* **26**, 50207 (2012).
49. Nitsche, F., Doert, T. & Ruck, M. Tetragonal to orthorhombic phase transition of GdFeAsO studied by single-crystal x-ray diffraction. *Solid State Sci.* **19**, 162 (2013).
50. Wang, X. & Fernandes, R. M. Impact of local-moment fluctuations on the magnetic degeneracy of iron arsenide superconductors. *Phys. Rev. B-Condens. Matter Mater. Phys.* **89**, 144502 (2014).
51. Christensen, M. H., Scherer, D. D., Kotetes, P. & Andersen, B. M. Role of multiorbital effects in the magnetic phase diagram of iron pnictides. *Phys. Rev. B* **96**, 014523 (2017).
52. Cvetkovic, V. & Vafeek, O. Space group symmetry, spin-orbit coupling, and the low-energy effective hamiltonian for iron-based superconductors. *Phys. Rev. B-Condens. Matter Mater. Phys.* **88**, 134510 (2013).
53. Yin, Z. P., Haule, K. & Kotliar, G. Kinetic frustration and the nature of the magnetic and paramagnetic states in iron pnictides and iron chalcogenides. *Nat. Mater.* **10**, 932 (2011).
54. Lu, D. H. et al. Electronic structure of the iron-based superconductor LaOFeP. *Nature* **455**, 81 (2008).
55. Reiss, P. et al. Suppression of electronic correlations by chemical pressure from FeSe to FeS. *Phys. Rev. B* **96**, 121103 (2017).
56. Xu, N. et al. Effects of Ru substitution on electron correlations and fermi-surface dimensionality in Ba(Fe_{1-x}Ru_x)₂As₂. *Phys. Rev. B - Condens. Matter Mater. Phys.* **86**, 64505 (2012).
57. Meier, W. R. et al. Anisotropic thermodynamic and transport properties of single-crystalline CaKFe₄As₄. *Phys. Rev. B* **94**, 064501 (2016).
58. Usui, H. & Kuroki, K. Maximizing the Fermi-surface multiplicity optimizes the superconducting state of iron pnictide compounds. *Phys. Rev. B-Condens. Matter Mater. Phys.* **84**, 024505 (2011).
59. Ren, Z. A. et al. Superconductivity and phase diagram in iron-based arsenic-oxides ReFeAsO_{1-δ} (Re = Rare-Earth Metal) without fluorine doping. *EPL* **83**, 17002 (2008).
60. Mukuda, H. et al. Doping dependence of normal-state properties in iron-based oxypnictide superconductor LaFeAsO_{1-y} Probed by ⁵⁷Fe-NMR and ⁷⁵As-NMR/NQR. *J. Phys. Soc. Japan* **78**, 084717 (2009).
61. Vavilov, M. G. & Chubukov, A. V. Phase diagram of iron pnictides if doping acts as a source of disorder. *Phys. Rev. B-Condens. Matter Mater. Phys.* **84**, 214521 (2011).
62. Fernandes, R. M., Vavilov, M. G. & Chubukov, A. V. Enhancement of T_c by disorder in underdoped iron pnictide superconductors. *Phys. Rev. B-Condens. Matter Mater. Phys.* **85**, 140512 (2012).
63. Dolgov, O. V., Golubov, A. A. & Parker, D. Microwave response of superconducting pnictides: extended s_x Scenario. *N. J. Phys.* **11**, 75012 (2009).
64. Vorontsov, A. B., Vavilov, M. G. & Chubukov, A. V. Superfluid density and penetration depth in the iron pnictides. *Phys. Rev. B-Condens. Matter Mater. Phys.* **79**, 140507 (2009).
65. Bang, Y. Superfluid density of the ±s-wave state for the iron-based superconductors. *EPL* **86**, 47001 (2009).
66. Vildosola, V., Pourvorskii, L., Arita, R., Biermann, S. & Georges, A. Bandwidth and fermi surface of iron oxypnictides: covalency and sensitivity to structural changes. *Phys. Rev. B - Condens. Matter Mater. Phys.* **78**, 064518 (2008).
67. Arnold, O. et al. Mantid—Data analysis and visualization package for neutron scattering and μSR experiments. *Nuclear Instruments and Methods in Physics Research Section A: Accelerators, Spectrometers, Detectors and Associated Equipment* **764**, 156–166 (2014).
68. Toby, B. H. EXPGUI, a graphical user interface for GSAS. *J. Appl. Crystallogr.* **34**, 210 (2001).
69. Toby, B. H. & Von Dreele, R. B. GSAS-II: The genesis of a modern open-source all purpose crystallography software package. *J. Appl. Crystallogr.* **46**, 544 (2013).
70. Sannigrahi, J. et al. Magnetic states of Ni-Mn-Sn based shape memory alloy: a combined muon spin relaxation and neutron diffraction study. *Phys. Rev. B* **99**, 224401 (2019).
71. Dalmas De Réotier, P. & Yaouanc, A. Muon spin rotation and relaxation in magnetic materials. *J. Phys. Condens. Matter* **9**, 9113 (1997).

Acknowledgements

This work was primarily supported by the US Department of Energy, Office of Science, Basic Energy Sciences, Materials Science and Engineering Division. This research used resources of the Advanced Photon Source, a U.S. Department of Energy (DOE) Office of Science User Facility, operated for the DOE Office of Science by Argonne National Laboratory under Contract No. DE-AC02-06CH11357. A portion of this research used resources at the Spallation Neutron Source, a DOE Office of Science User Facility operated by the Oak Ridge National Laboratory. Experiments at the ISIS Pulsed Neutron and Muon Source were supported by beamtime allocation from the Science and Technology Facilities Council. Theory work (MHC and RMF) was supported by the US Department of Energy, Office of Science, Basic Energy Sciences, Materials Sciences and Engineering Division, under Award No. DE-SC0020045.

Author contributions

R.S. performed the synthesis, participated in all experiments and performed data analysis. D.K., P.M. and K.Y. participated in experiments at ISIS and assisted with data analysis on those experiments. S.L. participated in experiments at the Advanced Photon Source. M.C. and R.F. developed the theoretical model. D. Phelan assisted with magnetic susceptibility measurements. D.Y.C. supervised sample preparation. R.O. and S.R. supervised the project and participated in experiments at the Spallation Neutron Source. O.C. supervised the project, participated in all experiments, and assisted with data analysis. All authors contributed to the preparation of the manuscript.

Competing interests

The authors declare no competing interests.

Additional information

Supplementary information The online version contains supplementary material available at <https://doi.org/10.1038/s42005-022-00911-5>.

Correspondence and requests for materials should be addressed to Omar Chmaissem.

Peer review information *Communications Physics* thanks Hans-Henning Klauff, William Meier and the other, anonymous, reviewer(s) for their contribution to the peer review of this work.

Reprints and permission information is available at <http://www.nature.com/reprints>

Publisher's note Springer Nature remains neutral with regard to jurisdictional claims in published maps and institutional affiliations.



Open Access This article is licensed under a Creative Commons Attribution 4.0 International License, which permits use, sharing, adaptation, distribution and reproduction in any medium or format, as long as you give appropriate credit to the original author(s) and the source, provide a link to the Creative Commons license, and indicate if changes were made. The images or other third party material in this article are included in the article's Creative Commons license, unless indicated otherwise in a credit line to the material. If material is not included in the article's Creative Commons license and your intended use is not permitted by statutory regulation or exceeds the permitted use, you will need to obtain permission directly from the copyright holder. To view a copy of this license, visit <http://creativecommons.org/licenses/by/4.0/>.

© UChicago Argonne, LLC, Operator of Argonne National Laboratory 2022